The Astrophysical Journal, 716:1178–1190, 2010 June 20 doi:10.1088/0004-637X/716/2/1178

FERMI OBSERVATIONS OF GRB 090510: A SHORT–HARD GAMMA-RAY BURST WITH AN ADDITIONAL, HARD POWER-LAW COMPONENT FROM 10 keV TO GeV ENERGIES

M. Ackermann[1], K. Asano[2], W. B. Atwood[3], M. Axelsson[4,5,6], L. Baldini[7], J. Ballet[8], G. Barbiellini[9,10], M. G. Baring[11], D. Bastieri[12,13], K. Bechtol[1], R. Bellazzini[7], B. Berenji[1], P. N. Bhat[14], E. Bissaldi[15], R. D. Blandford[1], E. D. Bloom[1], E. Bonamente[16,17], A. W. Borgland[1], A. Bouvier[1], J. Bregeon[7], A. Brez[7], M. S. Briggs[14], M. Brigida[18,19], P. Bruel[20], S. Buson[12], G. A. Caliandro[21], R. A. Cameron[1], P. A. Caraveo[22], S. Carrigan[13], J. M. Casandjian[8], C. Cecchi[16,17], Ö. Çelik[23,24,25], E. Charles[1], J. Chiang[1], S. Ciprini[17], R. Claus[1], J. Cohen-Tanugi[26], V. Connaughton[14], J. Conrad[6,27,65], C. D. Dermer[28], F. de Palma[18,19], B. L. Dingus[29], E. do Couto e Silva[1], P. S. Drell[1], R. Dubois[1], D. Dumora[30,31], C. Farnier[26], C. Favuzzi[18,19], S. J. Fegan[20], J. Finke[28,32], W. B. Focke[1], M. Frailis[33,34], Y. Fukazawa[35], P. Fusco[18,19], F. Gargano[19], D. Gasparrini[36], N. Gehrels[23], S. Germani[16,17], N. Giglietto[18,19], F. Giordano[18,19], T. Glanzman[1], G. Godfrey[1], J. Granot[37], I. A. Grenier[8], M.-H. Grondin[30,31], J. E. Grove[28], S. Guiriec[14], D. Hadasch[38], A. K. Harding[23], E. Hays[23], D. Horan[20], R. E. Hughes[39], G. Jóhannesson[1], W. N. Johnson[28], T. Kamae[1], H. Katagiri[35], J. Kataoka[40], N. Kawai[41,42], R. M. Kippen[29], J. Knödlseder[43], D. Kocevski[1], C. Kouveliotou[44], M. Kuss[7], J. Lande[1], L. Latronico[7], M. Lemoine-Goumard[30,31], M. Llena Garde[6,27], F. Longo[9,10], F. Loparco[18,19], B. Lott[30,31], M. N. Lovellette[28], P. Lubrano[16,17], A. Makeev[28,45], M. N. Mazziotta[19], J. E. McEnery[23,46], S. McGlynn[6,47], C. Meegan[48], P. Mészáros[49], P. F. Michelson[1], W. Mitthumsiri[1], T. Mizuno[35], A. A. Moiseev[24,46], C. Monte[18,19], M. E. Monzani[1], E. Moretti[9,10], A. Morselli[50], I. V. Moskalenko[1], S. Murgia[1], H. Nakajima[41], T. Nakamori[41], P. L. Nolan[1], J. P. Norris[51], E. Nuss[26], M. Ohno[52], T. Ohsugi[53], N. Omodei[1], E. Orlando[15], J. F. Ormes[51], M. Ozaki[52], W. S. Paciesas[14], D. Paneque[1], J. H. Panetta[1], D. Parent[28,30,31,45], V. Pelassa[26], M. Pepe[16,17], M. Pesce-Rollins[7], F. Piron[26], R. Preece[14], S. Rainò[18,19], R. Rando[12,13], M. Razzano[7], S. Razzaque[28,32], A. Reimer[1,54], S. Ritz[3], A. Y. Rodriguez[21], M. Roth[55], F. Ryde[6,47], H. F.-W. Sadrozinski[3], A. Sander[39], J. D. Scargle[56], T. L. Schalk[3], C. Sgrò[7], E. J. Siskind[57], P. D. Smith[39], G. Spandre[7], P. Spinelli[18,19], M. Stamatikos[23,39], F. W. Stecker[23], M. S. Strickman[28], D. J. Suson[58], H. Tajima[1], H. Takahashi[53], T. Takahashi[52], T. Tanaka[1], J. B. Thayer[1], J. G. Thayer[1], D. J. Thompson[23], L. Tibaldo[8,12,13,66], K. Toma[49], D. F. Torres[38,21], G. Tosti[16,17], A. Tramacere[1,59,60], Y. Uchiyama[1], T. Uehara[35], T. L. Usher[1], A. J. van der Horst[44,67], V. Vasileiou[24,25], N. Vilchez[43], V. Vitale[50,61], A. von Kienlin[15], A. P. Waite[1], P. Wang[1], C. Wilson-Hodge[44], B. L. Winer[39], X. F. Wu[49,62,63], R. Yamazaki[35], Z. Yang[6,27], T. Ylinen[6,47,64], and M. Ziegler[3]

[1] W. W. Hansen Experimental Physics Laboratory, Kavli Institute for Particle Astrophysics and Cosmology, Department of Physics and SLAC National Accelerator Laboratory, Stanford University, Stanford, CA 94305, USA; jchiang@slac.stanford.edu
[2] Interactive Research Center of Science, Tokyo Institute of Technology, Meguro City, Tokyo 152-8551, Japan
[3] Santa Cruz Institute for Particle Physics, Department of Physics and Department of Astronomy and Astrophysics, University of California at Santa Cruz, Santa Cruz, CA 95064, USA
[4] Department of Astronomy, Stockholm University, SE-106 91 Stockholm, Sweden
[5] Lund Observatory, SE-221 00 Lund, Sweden
[6] The Oskar Klein Centre for Cosmoparticle Physics, AlbaNova, SE-106 91 Stockholm, Sweden
[7] Istituto Nazionale di Fisica Nucleare, Sezione di Pisa, I-56127 Pisa, Italy
[8] Laboratoire AIM, CEA-IRFU/CNRS/Université Paris Diderot, Service d'Astrophysique, CEA Saclay, 91191 Gif sur Yvette, France
[9] Istituto Nazionale di Fisica Nucleare, Sezione di Trieste, I-34127 Trieste, Italy
[10] Dipartimento di Fisica, Università di Trieste, I-34127 Trieste, Italy
[11] Department of Physics and Astronomy, Rice University, MS-108, P.O. Box 1892, Houston, TX 77251, USA
[12] Istituto Nazionale di Fisica Nucleare, Sezione di Padova, I-35131 Padova, Italy
[13] Dipartimento di Fisica "G. Galilei," Università di Padova, I-35131 Padova, Italy
[14] Center for Space Plasma and Aeronomic Research (CSPAR), University of Alabama in Huntsville, Huntsville, AL 35899, USA; sylvain.guiriec@lpta.in2p3.fr
[15] Max-Planck Institut für extraterrestrische Physik, 85748 Garching, Germany
[16] Istituto Nazionale di Fisica Nucleare, Sezione di Perugia, I-06123 Perugia, Italy
[17] Dipartimento di Fisica, Università degli Studi di Perugia, I-06123 Perugia, Italy
[18] Dipartimento di Fisica "M. Merlin" dell'Università e del Politecnico di Bari, I-70126 Bari, Italy
[19] Istituto Nazionale di Fisica Nucleare, Sezione di Bari, 70126 Bari, Italy
[20] Laboratoire Leprince-Ringuet, École polytechnique, CNRS/IN2P3, Palaiseau, France
[21] Institut de Ciencies de l'Espai (IEEC-CSIC), Campus UAB, 08193 Barcelona, Spain
[22] INAF-Istituto di Astrofisica Spaziale e Fisica Cosmica, I-20133 Milano, Italy
[23] NASA Goddard Space Flight Center, Greenbelt, MD 20771, USA
[24] Center for Research and Exploration in Space Science and Technology (CRESST) and NASA Goddard Space Flight Center, Greenbelt, MD 20771, USA
[25] Department of Physics and Center for Space Sciences and Technology, University of Maryland Baltimore County, Baltimore, MD 21250, USA
[26] Laboratoire de Physique Théorique et Astroparticules, Université Montpellier 2, CNRS/IN2P3, Montpellier, France
[27] Department of Physics, Stockholm University, AlbaNova, SE-106 91 Stockholm, Sweden
[28] Space Science Division, Naval Research Laboratory, Washington, DC 20375, USA
[29] Los Alamos National Laboratory, Los Alamos, NM 87545, USA
[30] CNRS/IN2P3, Centre d'Études Nucléaires Bordeaux Gradignan, UMR 5797, Gradignan 33175, France
[31] Centre d'Études Nucléaires Bordeaux Gradignan, Université de Bordeaux, UMR 5797, Gradignan 33175, France
[32] National Research Council Research Associate, National Academy of Sciences, Washington, DC 20001, USA
[33] Dipartimento di Fisica, Università di Udine and Istituto Nazionale di Fisica Nucleare, Sezione di Trieste, Gruppo Collegato di Udine, I-33100 Udine, Italy
[34] Osservatorio Astronomico di Trieste, Istituto Nazionale di Astrofisica, I-34143 Trieste, Italy
[35] Department of Physical Sciences, Hiroshima University, Higashi-Hiroshima, Hiroshima 739-8526, Japan
[36] Agenzia Spaziale Italiana (ASI) Science Data Center, I-00044 Frascati (Roma), Italy
[37] Centre for Astrophysics Research, University of Hertfordshire, College Lane, Hatfield AL10 9AB, UK; j.granot@herts.ac.uk

[38] Institució Catalana de Recerca i Estudis Avançats (ICREA), Barcelona, Spain
[39] Department of Physics, Center for Cosmology and Astro-Particle Physics, The Ohio State University, Columbus, OH 43210, USA
[40] Research Institute for Science and Engineering, Waseda University, 3-4-1, Okubo, Shinjuku, Tokyo 169-8555, Japan
[41] Department of Physics, Tokyo Institute of Technology, Meguro City, Tokyo 152-8551, Japan
[42] Cosmic Radiation Laboratory, Institute of Physical and Chemical Research (RIKEN), Wako, Saitama 351-0198, Japan
[43] Centre d'Étude Spatiale des Rayonnements, CNRS/UPS, BP 44346, F-30128 Toulouse Cedex 4, France
[44] NASA Marshall Space Flight Center, Huntsville, AL 35812, USA
[45] George Mason University, Fairfax, VA 22030, USA
[46] Department of Physics and Department of Astronomy, University of Maryland, College Park, MD 20742, USA
[47] Department of Physics, Royal Institute of Technology (KTH), AlbaNova, SE-106 91 Stockholm, Sweden
[48] Universities Space Research Association (USRA), Columbia, MD 21044, USA
[49] Department of Astronomy and Astrophysics, Pennsylvania State University, University Park, PA 16802, USA
[50] Istituto Nazionale di Fisica Nucleare, Sezione di Roma "Tor Vergata," I-00133 Roma, Italy
[51] Department of Physics and Astronomy, University of Denver, Denver, CO 80208, USA
[52] Institute of Space and Astronautical Science, JAXA, 3-1-1 Yoshinodai, Sagamihara, Kanagawa 229-8510, Japan; ohno@astro.isas.jaxa.jp
[53] Hiroshima Astrophysical Science Center, Hiroshima University, Higashi-Hiroshima, Hiroshima 739-8526, Japan
[54] Institut für Astro- und Teilchenphysik and Institut für Theoretische Physik, Leopold-Franzens-Universität Innsbruck, A-6020 Innsbruck, Austria
[55] Department of Physics, University of Washington, Seattle, WA 98195-1560, USA
[56] Space Sciences Division, NASA Ames Research Center, Moffett Field, CA 94035-1000, USA
[57] NYCB Real-Time Computing Inc., Lattingtown, NY 11560-1025, USA
[58] Department of Chemistry and Physics, Purdue University Calumet, Hammond, IN 46323-2094, USA
[59] Consorzio Interuniversitario per la Fisica Spaziale (CIFS), I-10133 Torino, Italy
[60] INTEGRAL Science Data Centre, CH-1290 Versoix, Switzerland
[61] Dipartimento di Fisica, Università di Roma "Tor Vergata," I-00133 Roma, Italy
[62] Joint Center for Particle Nuclear Physics and Cosmology (J-CPNPC), Nanjing 210093, China
[63] Purple Mountain Observatory, Chinese Academy of Sciences, Nanjing 210008, China
[64] School of Pure and Applied Natural Sciences, University of Kalmar, SE-391 82 Kalmar, Sweden
Received 2010 February 5; accepted 2010 May 2; published 2010 May 27

ABSTRACT

We present detailed observations of the bright short–hard gamma-ray burst GRB 090510 made with the Gamma-ray Burst Monitor (GBM) and Large Area Telescope (LAT) on board the *Fermi* observatory. GRB 090510 is the first burst detected by the LAT that shows strong evidence for a deviation from a Band spectral fitting function during the prompt emission phase. The time-integrated spectrum is fit by the sum of a Band function with $E_{\rm peak} = 3.9 \pm 0.3$ MeV, which is the highest yet measured, and a hard power-law component with photon index -1.62 ± 0.03 that dominates the emission below ≈20 keV and above ≈100 MeV. The onset of the high-energy spectral component appears to be delayed by ∼0.1 s with respect to the onset of a component well fit with a single Band function. A faint GBM pulse and a LAT photon are detected 0.5 s before the main pulse. During the prompt phase, the LAT detected a photon with energy $30.5^{+5.8}_{-2.6}$ GeV, the highest ever measured from a short GRB. Observation of this photon sets a minimum bulk outflow Lorentz factor, $\Gamma \gtrsim 1200$, using simple $\gamma\gamma$ opacity arguments for this GRB at redshift $z = 0.903$ and a variability timescale on the order of tens of ms for the ≈100 keV–few MeV flux. Stricter high confidence estimates imply $\Gamma \gtrsim 1000$ and still require that the outflows powering short GRBs are at least as highly relativistic as those of long-duration GRBs. Implications of the temporal behavior and power-law shape of the additional component on synchrotron/synchrotron self-Compton, external-shock synchrotron, and hadronic models are considered.

Key words: gamma-ray burst: individual (GRB 090510) – radiation mechanisms: non-thermal

Online-only material: color figures

1. INTRODUCTION

A difficulty in trying to understand gamma-ray bursts (GRBs) is that, at least in terms of the temporal structure of their emission, all GRBs differ. When the overall timescales of the emission are considered, however, a pattern does emerge. The durations of the ∼100 keV–MeV emission from GRBs form a bimodal distribution and hence are divided into two classes, namely, the short- and long-duration bursts. The short bursts formally have durations <2 s with typical values around ∼0.2 s, whereas the long bursts have a distribution that peaks around ∼30 s with a tail extending to several hundreds of seconds (Kouveliotou et al. 1993).

Although the physics of their gamma-ray emission is not well understood, these two classes of bursts likely originate from distinct types of progenitor systems (Lee & Ramirez-Ruiz 2007; Woosley & Bloom 2006). Long-duration bursts are thought to be produced by the core collapse of massive stars as evidenced by the direct association of several nearby GRBs ($z < 0.3$) with SN Ib/c events (Woosley & Bloom 2006). Consistent with this, the afterglow counterparts of long-duration GRBs tend to lie in star-forming regions of low mass, irregular galaxies (Kocevski et al. 2009). By contrast, short-duration GRBs have been associated with both early- and late-type host galaxies, in proportions that reflect the underlying field galaxy distribution (Berger 2009). In the prevailing model for short bursts, they are produced in merger events of a compact binary system composed of two

[65] Royal Swedish Academy of Sciences Research Fellow, funded by a grant from the K. A. Wallenberg Foundation.
[66] Partially supported by the International Doctorate on Astroparticle Physics (IDAPP) program.
[67] NASA Postdoctoral Program Fellow, USA.

neutron stars or a neutron star/black hole pair and so would tend to originate from older stellar populations.

With the launch and successful operation of the *Fermi Gamma-ray Space Telescope*, a wider observational window has been opened through which a greater understanding of GRBs may be obtained. The Large Area Telescope (LAT) aboard *Fermi* provides significantly greater energy coverage (20 MeV to >300 GeV), field of view (2.4 sr), and effective area (8000 cm^2 at 1 GeV) than its predecessor EGRET (Atwood et al. 2009). Owing to its substantially lower dead time (26 μs versus 100 ms for EGRET), the LAT can probe the temporal structure of even the shortest GRBs. In addition, the LAT can localize GRBs with sufficiently high precision to enable follow-up observations by *Swift* and ground-based observatories; and at energies $\gtrsim$few GeV, the LAT can distinguish GRB photons from background with little ambiguity. The Gamma-ray Burst Monitor (GBM), the other science instrument on *Fermi*, comprises an array of 12 sodium iodide (NaI) scintillators and two bismuth germanate (BGO) scintillators and can detect gamma rays from 8 keV to 40 MeV over the full unocculted sky. The combined capabilities of the LAT and GBM enable *Fermi* to measure the spectral parameters of GRBs over seven decades in energy. For sufficiently bright bursts, time-resolved spectral analysis is possible over the entire energy range.

The *Fermi* observations of the short gamma-ray burst, GRB 090510, take full advantage of the GBM and LAT capabilities. The LAT emission shows temporal structure on timescales as short as 20 ms. In addition to the usual Band function component (Band et al. 1993), spectral fits reveal a hard power-law component emerging in the LAT band 0.1 s after the onset of the main prompt emission in the GBM band. Moreover, a ≈0.2 s delay is observed between the brightening of the ≈200 MeV–GeV emission with respect to the strong count increases in the NaI and BGO. These behaviors present severe challenges for emission models of GRBs.

A photon with energy $30.5^{+5.8}_{-2.6}$ GeV was detected by the LAT 0.829 s after the GBM trigger. This event arrived during the prompt phase and is temporally coincident with a sharp feature in the GBM and LAT light curves. Given this energy, the temporal structure of the burst light curve and the known distance to the burst, Abdo et al. (2009a) have used this photon and its arrival time to set limits on a possible linear energy dependence of the propagation speed of photons due to Lorentz-invariance violation that would require a quantum-gravity mass scale significantly above the Planck mass. Similar to several of the long bursts seen by the LAT, GRB 090510 shows a high-energy extended emission component that is detected by the LAT as late as 200 s after the GBM trigger. In the context of GRB outflow models, the properties of this GeV emission and the optical and X-ray afterglow observations by *Swift* place significant constraints on possible internal and external shock models for the late time emission of this source (Ghirlanda et al. 2010; De Pasquale et al. 2010; Corsi et al. 2009; Gao et al. 2009; Kumar & Barniol Duran 2009b).

In this paper, we report on and discuss the GBM and LAT observations of GRB 090510 during the prompt emission phase. In Section 2, we give the basic observational details. In Section 3, we present a timing analysis, including discussion of its designation as a short-hard GRB and a cross-correlation analysis between various energy bands to characterize any energy-dependent temporal lags. In Section 4, we perform spectral analyses of both the time-integrated and the time-resolved data; and we demonstrate the significance of the additional power-law component and how the spectra evolve over the course of the burst. In Section 5, we derive a lower limit on the bulk Lorentz factor given the variability timescales and observations of the highest energy photons, describe the constraints imposed on leptonic, hadronic, and other models of the prompt emission, and discuss implications of the detection of the 30.5 GeV photon for models of the extragalactic background light (EBL). Finally, we summarize our results in Section 6.

2. BASIC OBSERVATIONS

On 2009 May 10 at 00:22:59.97 UT (hereafter T_0), both the GBM and LAT instruments triggered on GRB 090510 (trigger 263607781). During the first second after the trigger, the LAT detected 62 "transient class" events with energies >100 MeV and within 10° of the *Swift* UVOT position (Kuin & Hoversten 2009) and 12 events above 1 GeV. In the first minute post-trigger, the LAT detected 191 events above 100 MeV and 30 above 1 GeV. From spectral fits to the time-integrated emission over the time range $T_0 + 0.5$ s to $T_0 + 1.0$ s (see Section 4), the fluence of the burst is $(5.03 \pm 0.25) \times 10^{-5}$ erg cm^{-2} in the 10 keV to30 GeV band. In the 15–150 keV band, the fluence is $(4.08 \pm 0.07) \times 10^{-7}$ erg cm^{-2}.

Other detections of the prompt emission were made by *Swift* (Hoversten et al. 2009), *AGILE* (Longo et al. 2009), Konus-*Wind* (Golenetskii et al. 2009), *Suzaku* WAM (Ohmori et al. 2009), and INTEGRAL-ACS. The *Swift* UVOT instrument measured the position of the optical afterglow counterpart to be R.A.(J2000), decl.(J2000) = $22^h14^m12\overset{s}{.}5$, $-26°34'59\overset{''}{.}2$ (Kuin & Hoversten 2009). Follow-up optical spectroscopy taken 3.5 days later by VLT/FORS2 measured [O II] and Hβ emission lines at a common redshift of $z = 0.903 \pm 0.001$ (McBreen et al. 2010). Using standard cosmological parameters ($[\Omega_\Lambda, \Omega_M, h] = [0.73, 0.27, 0.71]$), this corresponds to a luminosity distance of $d_L = 1.80 \times 10^{28}$ cm and implies an apparent isotropic energy of $E_{iso} = (1.08 \pm 0.06) \times 10^{53}$ erg (10 keV–30 GeV, $T_0 + 0.5$ s to $T_0 + 1.0$ s). The optical afterglow was also detected by NOT (Olofsson et al. 2009) and GROND (Olivares et al. 2009). In the radio, however, only upper limits were obtained using the VLA (Frail & Chandra 2009).

The host galaxy of GRB 090510 was identified as a late-type elliptical or early-type spiral galaxy (Rau et al. 2009), in contrast to the dwarf irregular, star-forming galaxies that have been observed to harbor long-duration GRBs. This is consistent with the diverse types of hosts identified with short GRBs (e.g., Nakar 2007; Berger 2009).

3. TIMING ANALYSIS

In Figure 1, we plot the light curves from the different detectors in various energy bands. The upper two panels contain the data from the GBM NaI and BGO detectors in energy ranges 8–260 keV and 0.26–5 MeV, respectively. Both of these light curves show the precursor event at T_0 that caused the GBM trigger. The main part of the emission in both of these light curves starts approximately at $T_0 + 0.5$ s, though both light curves have a small but significant feature at $T_0 + 0.4$ s. The third panel displays all of the LAT events that passed the on board gamma filter and have at least one reconstructed track, and the fourth panel shows the light curve for the transient class selection at energies >100 MeV. In the bottom panel, the measured photon energies >1 GeV are plotted versus arrival time. The three LAT events in the >100 MeV light curve with arrival times in the interval $T_0 + 0$ s to $T_0 + 0.2$ s are very likely burst photons. Using

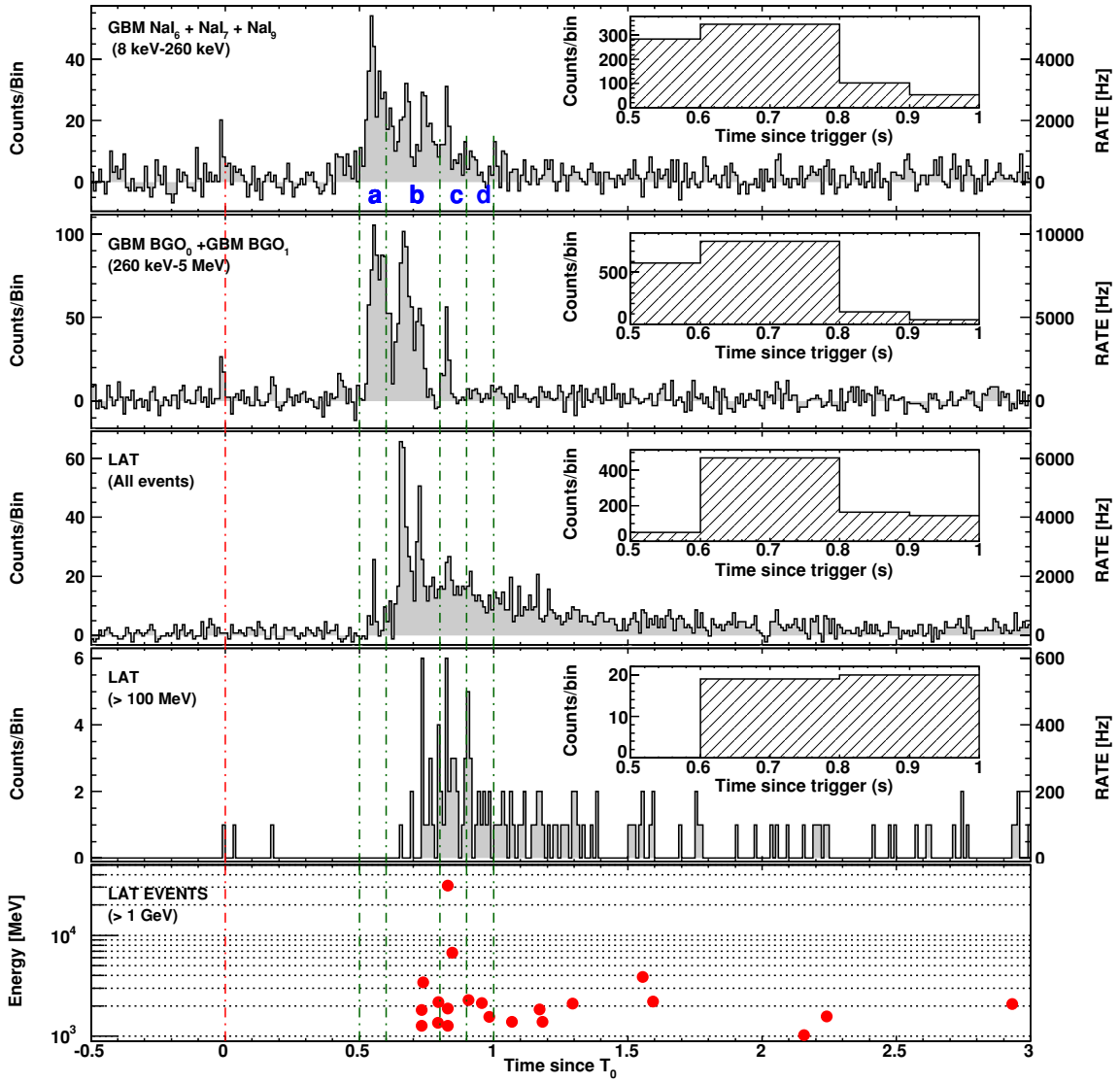

Figure 1. In the top four panels, the GBM and LAT light curves are shown, from lowest to highest energies. The bin size for all light curves is 0.01 s. In the bottom panel, the individual photon energies as a function of time are plotted. The red vertical dot-dashed line indicates the trigger time, and the black vertical dot-dashed lines indicate the boundaries used for the time-resolved spectral analysis. These intervals are labeled a, b, c, and d and correspond to $T_0 + 0.5$ s to $T_0 + 0.6$ s, $T_0 + 0.6$ s to $T_0 + 0.8$ s, $T_0 + 0.8$ s to $T_0 + 0.9$ s, and $T_0 + 0.9$ s to $T_0 + 1.$ s, respectively. The insets in the top four plots show the counts per bin within those time intervals. A previous version of this figure appeared in Abdo et al. (2009a).

(A color version of this figure is available in the online journal.)

the count rate in the LAT during the 200 s directly preceding T_0 as a measure of the background rate, the probability that these three photons would arise by accident is 1.2×10^{-6}.

Classification of GRBs as short versus long bursts is based on the T_{90} or T_{50} durations. The T_{90} (T_{50}) duration is defined as the time between accumulating 5% and 95% (25% and 75%) of the counts associated with the GRB. For the T_{90} and T_{50} durations of GRB 090510, we have applied the technique described in Koshut et al. (1996) to determine these quantities using data from multiple instruments (see Table 1). The cause of the wide range in T_{90} durations that we find is illustrated in Figure 2, where we have plotted the cumulative counts for two detectors, GBM/NaI6 and *Swift*/BAT, integrated over the energy ranges 50–300 keV and 50–350 keV, respectively. Ideally, the selection of the 0% and the 100% plateaus, which designate the onset and the end of the burst data accumulation, is unambiguous. However, when large background variations exist, the plateau selection is not unique as one can see in the upper panel of Figure 2. For the GBM data, the most conservative selection provides $T_{90} = 9.0$ s, while alternative detector selections give conservative lower values, down to 1.5 s (see Table 1). The *Swift*/BAT data (lower panel) have a much lower background and allow for a reasonably robust setting of the 100% level and yield $T_{90} = 4.0$ s. Similar plots have been obtained for other GBM detectors, as well as for the *INTEGRAL*-SPI and the *Suzaku*-WAM instruments. We find a narrower range of T_{50} values, compared to the T_{90} durations for the same data set. The latter are very sensitive to 5% background variations, while the former are more robust.

A common feature of long-duration GRBs is the trend for their higher energy photons (below ~1 MeV) to arrive before the lower energy ones (Norris et al. 2000). By contrast, short-duration GRBs typically show no evidence for lags between different energy ranges below 1 MeV (Norris & Bonnell 2006).

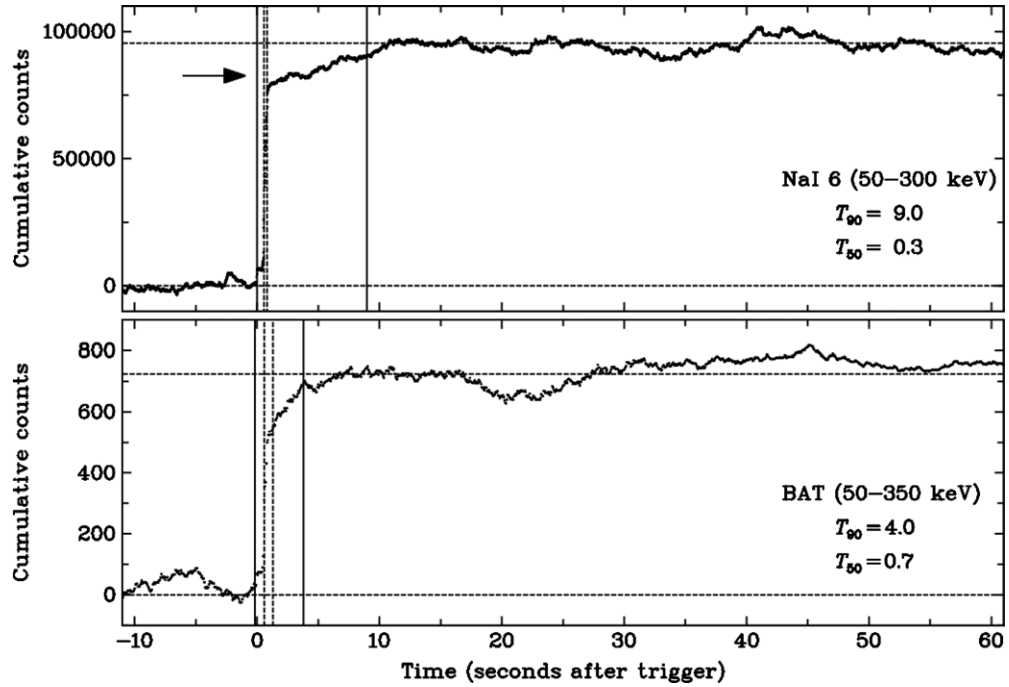

Figure 2. GRB 090510 T_{90} and T_{50} estimates using the GBM/NaI 6 (upper panel) and *Swift*/BAT (lower panel) detectors. The horizontal dashed lines indicate the 0% and 100% cumulative plateau levels, and the vertical solid and dashed lines indicate the T_{90} and T_{50} interval boundaries, respectively. The arrow in the upper panel indicates the lowest alternative 100% cumulative plateau level, which results in $T_{90} = 1.0$ s.

Table 1
Durations of GRB 090510 Detected with Different Instruments

Instrument	T_{90} (s)	T_{50} (s)	Energy Range
GBM/NaI 3	0.6	0.2	50–300 keV
GBM/NaI 6	9.0	0.3	50–300 keV
GBM/NaI 7	1.5	0.2	50–300 keV
GBM/NaI 3, 6, and 7	2.1	0.2	50–300 keV
Swift/BAT	4.0	0.7	50–350 keV
INTEGRAL-SPI	2.5	0.1	20 keV–10 MeV
Suzaku-WAM	5.8	0.5	50 keV–5 MeV

Therefore, since the T_{90} estimates in Table 1 span the formal 2 s divide between short- and long-duration bursts, the presence or absence of the "hard-to-soft" evolution seen in long bursts can help determine whether GRB 090510 should be classified as a short burst.

In order to estimate the energy-dependent lags for GRB 090510, we compute the cross-correlation function (CCF) between light curves for different energy bands among the various detectors. For these data, we define the CCF as a function of the lag τ using

$$\mathrm{CCF}(\tau) = \frac{\sum_{i=i_1}^{i_2}[f(t_i) - \bar{f}][g(t_i+\tau) - \bar{g})]}{\sqrt{\sum_{i=i_1}^{i_2}(f(t_i) - \bar{f})^2}\sqrt{\sum_{i=i_1}^{i_2}(g(t_i+\tau) - \bar{g})^2}}. \quad (1)$$

Here, $f(t_i)$ and $g(t_i)$ represent the content of the light curves we are comparing for bin i at time $t_i = i\,dt$ and bin size dt; $\bar{f}$ and $\bar{g}$ are the mean values of the two light curves evaluated over the time interval considered, (t_{i_1}, t_{i_2}); and the number of bins in each light curve is $N = i_2 - i_1 + 1$. At a given value of τ, Equation (1) is simply the linear correlation coefficient known as Pearson's r. If N is large, then r approximately follows a normal distribution with zero mean and standard deviation $1/\sqrt{N}$. In this case, the probability that a value greater than $|r| = |\mathrm{CCF}(\tau)|$ can arise by chance between two uncorrelated light curves is given by

$$P(|r|) = 1 - \mathrm{erf}(|r|\sqrt{N/2}), \quad (2)$$

where erf is the error function. Since the amplitude of the variations of the CCF are a strong function of the bin size, we instead plot the probability $P(\tau) = P(|\mathrm{CCF}(\tau)|)$ as a function of the lag τ. As we show in Figure 3, $P(\tau)$ is largely insensitive to the bin size and yields probabilities that we can easily interpret.

The emission in the LAT band is suppressed during $T_0 + 0.5$ s to $T_0 + 0.6$ s relative to the emission in the GBM band, and that suppression can dominate the CCF probability curves and appear as a relative lag. Since we also wish to determine if the individual pulses during the main part of the burst are correlated (i.e., where most of the "spiky" structure is seen), we consider two time intervals for our CCF studies: $T_0 + 0.5$ s to $T_0 + 1.5$ s and $T_0 + 0.6$ s to $T_0 + 0.9$ s. The former interval includes essentially all of the prompt phase emission, whereas the latter will be more useful for evaluating correlations in the spiky structure.

In the two leftmost plots in Figure 3, we show the CCF probabilities for the $T_0 + 0.6$ s to $T_0 + 0.9$ s interval. The upper plot compares the NaI data with the BGO data. The most significant correlation is at zero lag. Since the NaI data cover energies 8–260 keV and the BGO data cover 260 keV–5 MeV, this result shows that there is no evidence for an energy-dependent lag in the main Band function component of the prompt emission. This is consistent with GRB 090510 being a short burst. There is also a secondary minimum at $\tau = -0.075$ s, and this value for the lag corresponds to the rough separation between the pulses in the NaI and first two pulses in the BGO light curves and a shift of the BGO light curves by this amount to later times. In the lower left plot, no significant correlation at any lag is seen between the NaI light curve and the LAT data above 100 MeV; and we have performed Monte Carlo simulations and confirmed that the lack of a correlation is not simply due to the relatively low statistics in the LAT data. If indeed there is no

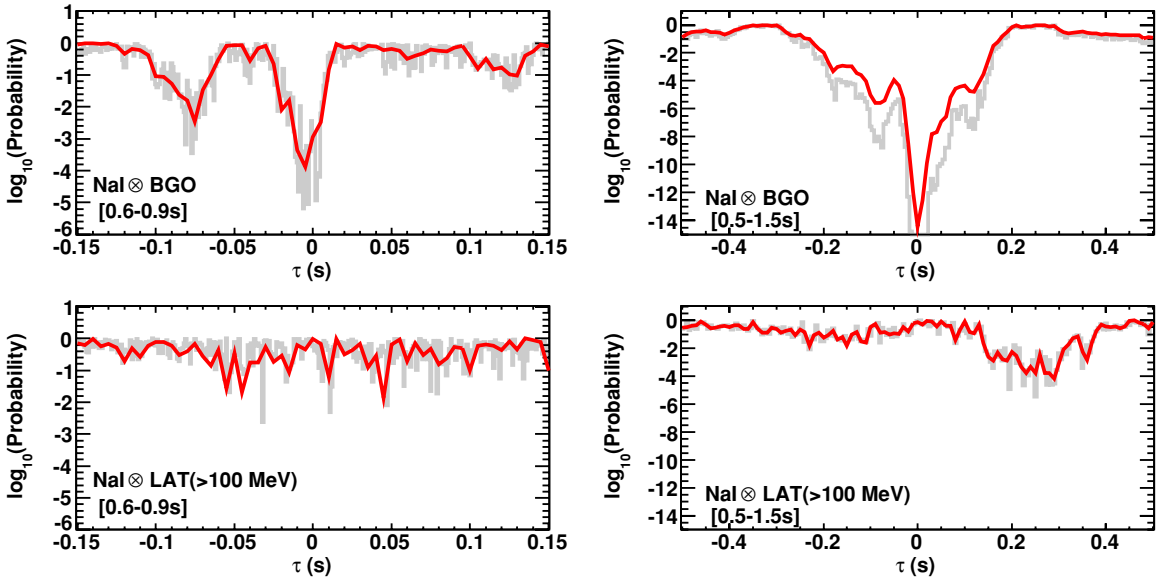

Figure 3. Cross-correlation function probability as a function of the lag τ for the specified light curve to follow the NaI light curve. The time intervals considered are indicated in the square brackets in each panel. The red curves correspond to time bins of size 0.01 s, and the gray curves correspond to 0.005 s. The fact that the probability curves are mostly independent of the bin size indicates that we are resolving all of the important features of the underlying variability.

(A color version of this figure is available in the online journal.)

such intrinsic temporal correlation, this would strongly suggest a different emission region from the Band spectral component, and no coupling between the observed emission from these two regions, e.g., via the external Compton mechanism: soft photons from the Band component upscattered to high energies by relativistic electrons in a different region. In the two rightmost plots of Figure 3, the results for the $T_0 + 0.5$ s to $T_0 + 1.5$ s interval are shown. The strong correlation at zero lag for the NaI versus BGO data is confirmed. In the NaI versus LAT data, the observed lag arises from the delayed onset of the >100 MeV emission by ∼0.2–0.3 s.

In addition to the lack of time lags for lower energy photons, short GRBs are also known to be substantially harder than long GRBs. For BATSE bursts, Kouveliotou et al. (1993) found a strong anticorrelation between the T_{90} duration and the hardness ratio of the burst. As we will show in the next section, GRB 090510 has the highest peak energy ever measured for any kind of burst and is undoubtedly one of the hardest GRBs seen. Given this result, the range of T_{90} and T_{50} durations we find, and the lack of any temporal lags for lower energy photons, we can safely consider GRB 090510 to be a short-duration GRB.

Finally, in Table 2, we give the shortest variability timescales, t_v, for the $T_0 + 0.6$ s to $T_0 + 0.8$ s and $T_0 + 0.8$ s to $T_0 + 0.9$ s intervals. These timescales will be used to compute the minimum bulk Lorentz factor implied by the observation of the highest energy ($\gtrsim$GeV) photons in those epochs (Section 5). The t_v values are given by the FWHM of the shortest pulse measured in any of the detectors for a given time interval.

4. SPECTRAL ANALYSIS

The spectral analysis included data from the most brightly illuminated GBM/NaI detectors, 3, 6, 7, 8, and 9, covering an energy range 8 keV–1 MeV, and from both GBM/BGO detectors, covering 200 keV–40 MeV. Since we wish to fit spectra on short timescales, we used the Time-Tagged Event (TTE) data with the energy overflow channels removed. The background for each GBM detector was found by fitting the data in 30 s time intervals that preceded and followed the prompt emission component by ∼2 s, using a polynomial function, then extrapolating to the times during the burst. Custom-made detector response files for the different GBM detectors were created using the *Swift*/UVOT location. The LAT photon data were extracted for energies 100 MeV–200 GeV and using an energy-dependent 95% point-spread function acceptance cone centered on the source, where we have increased the acceptance cone radius by adding in quadrature the uncertainty in the *Swift*/UVOT location. Appropriate for short timescale (≪1 ks) analyses, we used the "transient" class event selection and the corresponding instrument response functions known as P6_V3_TRANSIENT. The response matrix files were created using the `gtrspgen` tool from ScienceTools v9r15p2. The background during the burst was computed by averaging the LAT background over several orbits of the spacecraft during epochs when it had the same orbital position and pointing. The joint spectral fits were performed using the spectral analysis package RMFIT (version 3.1).

Table 2
$\Gamma_{\rm min}$ Values for the Shortest Timescale Pulses from GRB 090510

$T - T_0$ (s)	Spectrum	t_v (ms)	$E_{\rm max}$ (GeV)	$\Gamma_{\rm min}$[a]
0.6–0.8	Band + PL	14 ± 2	3.4	951 ± 38
0.6–0.8	PL[b]	14 ± 2	3.4	703 ± 34
0.8–0.9	Band[c]	12 ± 2	30.5	1324 ± 50
0.8–0.9	Band + PL	12 ± 2	30.5	1218 ± 61
0.8–0.9	PL[b]	12 ± 2	30.5	1083 ± 88

Notes.

[a] Uncertainty on $\Gamma_{\rm min}$ is associated with uncertainties in t_v and spectral flux only.

[b] Variability time t_v for power-law (PL) component is assumed to be the same as that derived from the BGO emission, which is described primarily by Band component.

[c] The Band-function-only fit gives a larger flux than the Band plus power-law fit in the portion of the spectrum where the highest energy γ rays typically interact; see Figure 5.

Table 3
Prompt Emission Spectral Fit Parameters

$T - T_0$ (s)	Model	Band Model				Power Law or Comptonized			CSTAT/dof
		A (10^{-2} cm^{-2} s^{-1} keV^{-1})	$E_{\rm peak}$ (MeV)	α	β	A at 1 GeV (10^{-9} cm^{-2} s^{-1} keV^{-1})	$E_{\rm pk}$ (MeV)	Index	
0.5–1.0	Band	$4.316^{+0.116}_{-0.115}$	$4.104^{+0.267}_{-0.263}$	$-0.75^{+0.03}_{-0.02}$	-2.40 ± 0.04	...	...	...	1016/970
	Band + PL	$3.188^{+0.269}_{-0.258}$	$3.936^{+0.280}_{-0.260}$	$-0.58^{+0.06}_{-0.05}$	$-2.83^{+0.14}_{-0.20}$	$2.426^{+0.531}_{-0.509}$	...	-1.62 ± 0.03	979/968
	Band + Comp	$3.203^{+0.281}_{-0.266}$	$4.002^{+0.285}_{-0.271}$	-0.59 ± 0.06	$2.94^{+0.18}_{-0.25}$	$3.011^{+0.697}_{-0.658}$	$8.71^{+\infty}_{-4.18}$	-1.60 ± 0.03	976/967
0.5–0.6	Band	$8.047^{+0.346}_{-0.344}$	$2.809^{+0.185}_{-0.174}$	-0.59 ± 0.04	< -5.0	...	...	...	840/971
0.6–0.8	Band + PL	$2.984^{+0.365}_{-0.341}$	$5.102^{+0.443}_{-0.400}$	-0.48 ± 0.07	$-3.09^{+0.21}_{-0.35}$	$1.862^{+0.719}_{-0.625}$	...	-1.66 ± 0.04	991/968
0.8–0.9	Band	$0.040^{+0.005}_{-0.004}$	$1.414^{+0.928}_{-0.536}$	$-1.00^{+0.11}_{-0.09}$	$-1.85^{+0.05}_{-0.06}$	...	...	...	886/970
	Band + PL	0.028 ± 0.006	$1.894^{+1.160}_{-0.718}$	$-0.86^{+0.17}_{-0.23}$	-3.09 (fixed)	$6.439^{+1.550}_{-1.230}$	...	$-1.54^{+0.07}_{-0.04}$	890/969
0.9–1.0	PL (LAT only)	...	...	...	...	$3.721^{+1.260}_{-1.080}$	...	$-1.92^{+0.20}_{-0.22}$	43/118

In Table 3, we show the results of joint spectral fits of the GBM and LAT data for the time-integrated and time-resolved data, including the definitions of the intervals used for spectral analysis. We define four intervals a, b, c, and d corresponding to $T_0+0.5$ s to $T_0+0.6$ s, $T_0+0.6$ s to $T_0+0.8$ s, $T_0+0.8$ s to $T_0+0.9$ s, and $T_0+0.9$ s to $T_0+1.$ s, respectively. The time-integrated spectrum from $T_0+0.5$ s to $T_0+1.0$ s shows a deviation from the standard Band function and can be adequately fit with the addition of a power-law spectral component,

$$n(E) = A\left(\frac{E}{1\,\mathrm{GeV}}\right)^{\lambda}, \quad (3)$$

or a Comptonized spectral component,

$$n(E) = A\left(\frac{E}{1\,\mathrm{GeV}}\right)^{\alpha}\exp\left(-\frac{E(2+\alpha)}{E_{\rm pk}}\right). \quad (4)$$

The Band function consists of two power laws that are smoothly joined near the peak photon energy, $E_{\rm peak}$. For our analyses, we use the Band function in the form

$$\begin{aligned} n(E) &= A\left(\frac{E}{100\,\mathrm{keV}}\right)^{\alpha}\exp\left(-\frac{E(2+\alpha)}{E_{\rm peak}}\right) \quad E < E_c, \\ &= A\left(\frac{(\alpha-\beta)E_{\rm peak}}{100\,\mathrm{keV}(2+\alpha)}\right)^{\alpha-\beta}\exp(\beta-\alpha) \\ &\quad \times\left(\frac{E}{100\,\mathrm{keV}}\right)^{\beta} \quad E \geqslant E_c, \end{aligned} \quad (5)$$

where $E_c = (\alpha-\beta)E_{\rm peak}/(2+\alpha)$ (Band et al. 1993).

For the time-integrated data, the peak energy of the Band component is $E_{\rm peak} = 3.9 \pm 0.3$ MeV. This is the highest peak energy ever measured in a GRB time-integrated spectrum. The addition of the power-law component with a photon index of -1.62 ± 0.03 significantly improves the fit by more than 5σ compared to a single Band function. This is the first short burst for which such a hard power-law component has been measured. The power-law component appears to extrapolate to energies well below $E_{\rm peak}$ and dominates the Band function emission below ≈20 keV, similar to the behavior seen in GRB 090902B (Abdo et al. 2009b). Figure 4 shows the counts spectrum of the time-integrated data and the Band function + power-law fit. In Figure 5, we plot this composite model as a νF_ν spectrum and also plot the separate contributions for each component.

For the time-resolved spectroscopy, we initially considered the data partitioned into 0.1 s time bins, starting at $T_0 + 0.5$ s. However, for the analyses we present here, we have combined the data in the $T_0 + 0.6$ s to $T_0 + 0.8$ s interval into a single bin in order to have sufficient counts at energies >100 MeV to constrain the fit of the LAT data. The parameters from the spectral fits to the selected intervals are given in Table 3. The Band component undergoes substantial evolution over the course of the prompt phase, starting out relatively soft with $E_{\rm peak} \approx 3$ MeV, evolving to a very hard spectrum with $E_{\rm peak} \approx 5$ MeV, accompanied by the appearance of the power-law component at >100 MeV, and then becoming softer again with $E_{\rm peak} \approx 2$ MeV. The extra power-law component hints at a similar sort of soft-hard-soft evolution, but these spectral changes do not appear to be commensurate with the Band component evolution (see Figure 5(b)).

5. DISCUSSION AND IMPLICATIONS

The emergence of a distinct high-energy spectral component in the prompt-phase spectrum of GRB 090510 establishes that a hard emission component in addition to a Band component is found in the short–hard class of GRBs. Hard power-law components are also found in three long-duration GRBs, namely, GRB 090902B (Abdo et al. 2009b), GRB 090926A (A. A. Abdo et al. 2010, in preparation), and GRB 941017 (González et al. 2003). In GRB 090510, the LAT data show that the γ-ray flux above 100 MeV brightens ≈0.2 s after the start of the bright phase of GBM emission. This behavior is similar, but on a shorter timescale, to the delayed onset in the long-duration GRB 080916C (Abdo et al. 2009c) and most other *Fermi* GRBs, including GRB 081024B, the first short GRB observed with the LAT (Abdo et al. 2010). Furthermore, GRB 090510 displays >100 MeV emission significantly extended beyond the duration of the GBM flux (De Pasquale et al. 2010), as observed in other *Fermi* GRBs and earlier from GRB 940217 with the EGRET instrument on the *Compton Observatory* (Hurley et al. 1994). These behaviors provide important constraints for high-energy emission models and could help answer whether the high-energy γ rays have a leptonic or hadronic origin.

Though the afterglow radiation in both long and short GRBs is probably nonthermal synchrotron emission from an external shock (Sari et al. 1998), the situation is less clear in the prompt and early afterglow phases when the GRB engine is most powerful. This radiation could be from the thermal photosphere made by the powerful relativistic wind (Mészáros et al. 2002; Pe'er et al. 2007), from magnetic reconnection in Poynting-flux dominated outflows (Lyutikov & Blandford 2003), or from nonthermal leptonic emissions formed by internal or external

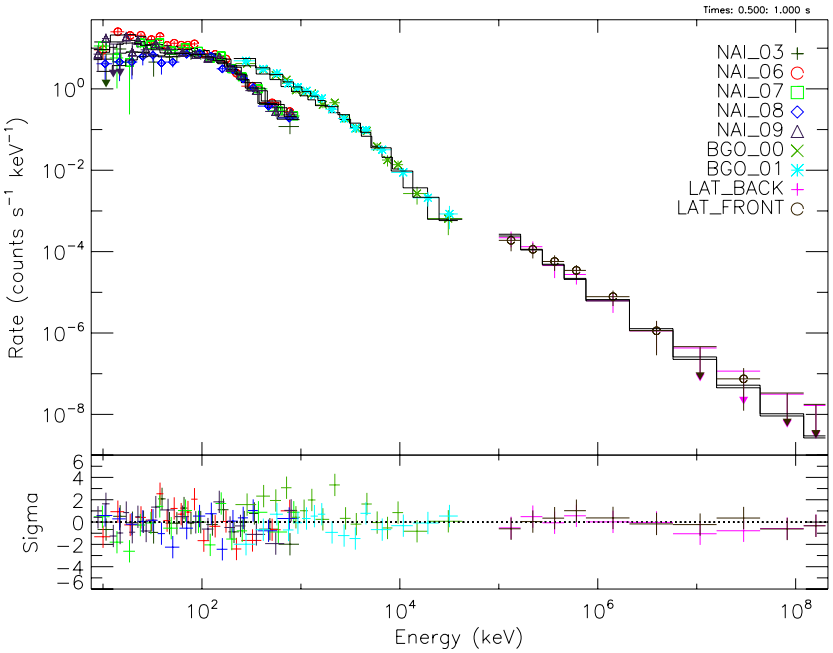

Figure 4. Counts spectrum for the time-integrated (T_0 + 0.5, T_0 + 1.0 s) data. The Band + power-law model has been fit to these data. See Table 3.
(A color version of this figure is available in the online journal.)

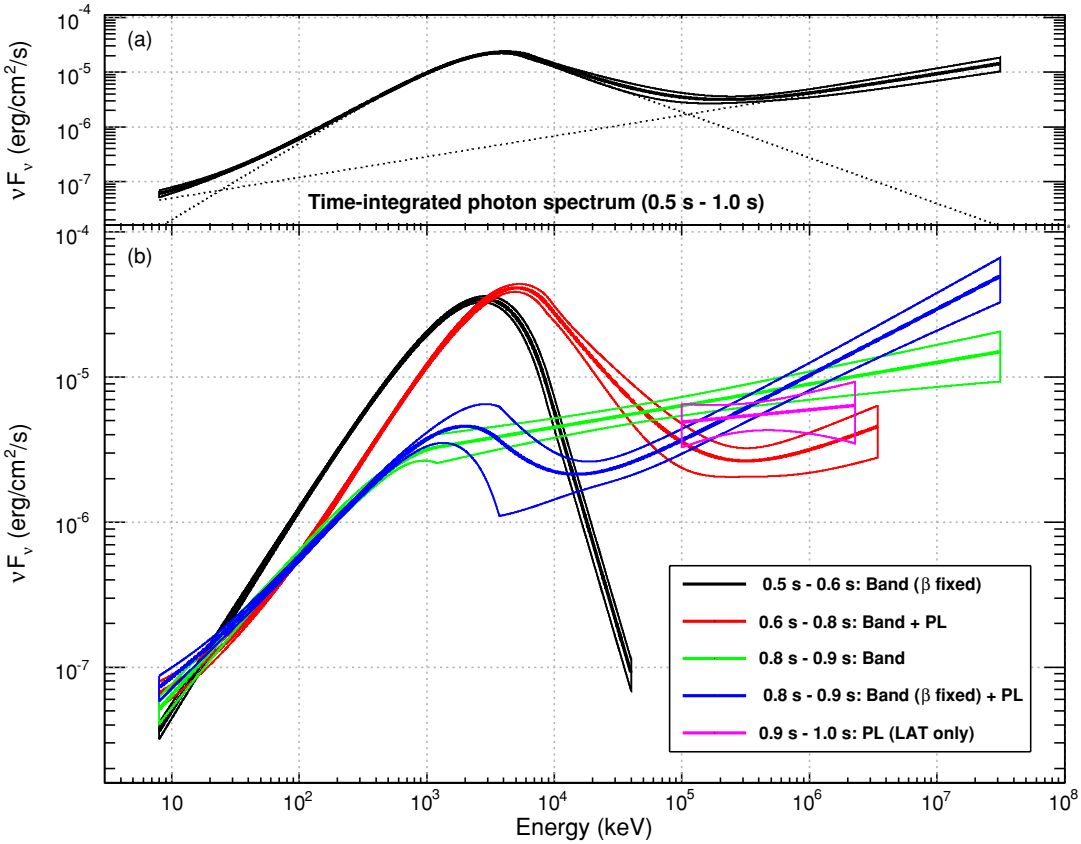

Figure 5. (a) Best-fit Band + power-law model for the time-integrated data plotted as a νF_ν spectrum. The two components are plotted separately and the sum is plotted as the heavy line. The $\pm 1\sigma$ error contours derived from the errors on the fit parameters are also shown. (b) The νF_ν model spectra (and $\pm 1\sigma$ error contours) plotted for the different time ranges given in Table 3.
(A color version of this figure is available in the online journal.)

shocks (e.g., Kumar & Barniol Duran 2009b; Ghirlanda et al. 2010; Corsi et al. 2009) in the relativistic jet of a GRB.

De Pasquale et al. (2010) describe and present models for the *Swift* and *Fermi* observations of GRB 090510 during the afterglow phase. Here, we consider the implications of the prompt phase and early afterglow emission for GRB 090510. After deriving the minimum bulk Lorentz factor $\Gamma_{\rm min}$ and considering the various uncertainties that enter into this calculation, we use the

observations to constrain leptonic synchrotron/synchrotron self-Compton (SSC) model and hadronic models of short-duration GRBs. We do not discuss a thermal photospheric interpretation for the *Fermi* results on GRB 090510. The photospheric interpretation overcomes the problem that the GBM spectra are harder than expected below $E_{\rm peak}$ with the simplest synchrotron emission model (which is only the case at $\gtrsim 2\sigma$ in GRB 090510 during interval b; see Table 3). Even if it explains much of the GBM emission, however, a different origin is needed for the separate hard spectral component observed at LAT energies. The coincident narrow spikes between the LAT all events and GBM light curves would not be easy to explain in a purely photospheric scenario, though Compton-scattered photospheric emission by internal shocked electrons could produce the coincident components (Toma et al. 2010).

5.1. Lower Limit on the Bulk Lorentz Factor

The use of γ-ray observations to constrain the bulk outflow speed of highly variable and energetic γ-ray emission from GRBs has been studied by many authors (e.g., Baring & Harding 1997; Lithwick & Sari 2001; Razzaque et al. 2004). A detailed derivation involves an integration over the photon spectrum to calculate the opacity of γ rays emitted from sources with idealized geometries (see supplementary information in Abdo et al. 2009c). A δ-function approximation for the $\gamma\gamma$ opacity constraint gives values of $\Gamma_{\rm min}$ accurate to $\sim$10% whenever the target photon spectrum is softer than $\nu F_\nu \propto \nu$. In this case, $\gamma\gamma$ opacity arguments for a γ-ray photon with energy ϵ_1, in $m_e c^2$ units, imply a minimum bulk Lorentz factor, defined by $\tau_{\gamma\gamma}(\epsilon_1) = 1$, of (e.g., Dondi & Ghisellini 1995; Nakar 2007)

$$\Gamma_{\rm min} \cong \left[\frac{\sigma_T d_L^2 (1+z)^2 f_{\hat{\epsilon}} \epsilon_1}{4 t_v m_e c^4}\right]^{1/6}, \quad \hat{\epsilon} = \frac{2\Gamma^2}{(1+z)^2 \epsilon_1}. \quad (6)$$

Here, f_ϵ is the νF_ν flux at photon energy $m_e c^2 \epsilon$, which is evaluated at $\epsilon = \hat{\epsilon}$ due to the peaking of the $\gamma\gamma$ cross section near threshold. While the local value of the photon index around $\hat{\epsilon}$ has some effect on the exact numerical coefficient, this effect is small provided that the target photon index is $< -1/2$. Because of the threshold condition used to relate the high-energy photon and the target photons, the solution to Equation (6) is iterative but quickly converges. We use this expression to estimate $\Gamma_{\rm min}$ from *Fermi* observations of GRB 090510 for comparison with more accurate calculations.

For interval b, during which a 3.4 GeV photon was detected, spectral analysis of GBM and LAT data during this episode reveals distinct Band-function and power-law components (Figure 5). The Band function has $E_{\rm peak} = 5.1$ MeV, $\alpha = -0.48$, and $\beta = -3.09$ (Table 3). The combined Band plus power-law fit reaches a peak νF_ν flux of $\approx 4 \times 10^{-5}$ erg cm^{-2} s^{-1}. Writing the variability timescale t_v(s) $= 0.01 t_{-2}$ s for 10 ms variability timescale, and $f_{\hat{\epsilon}} = 10^{-5} f_{-5}$ erg cm^{-2} s^{-1}, then Equation (6) gives $\Gamma_{\rm min} \cong 1100 (f_{-5}/t_{-2})^{1/6} \equiv 10^3 \Gamma_3$ with $\epsilon_1 = 3400/0.511 \cong 6650$. The target photon energy $\hat{\epsilon} \cong 2\Gamma_{\rm min}^2/(1+z)^2 \epsilon_1 \cong 110 (f_{-5}/t_{-2})^{1/3}$, or $\approx$50 MeV, corresponding to the Band β branch of the function. Depending on whether the 3.4 GeV photon is interacting with the total emission or just the photons in the power law, then $f_{-5} \approx 0.7$ or $f_{-5} \approx 0.1$, and $\Gamma_{\rm min} \cong 950$ or $\Gamma_{\rm min} \cong 720$, respectively. For interval c from $T_0 + 0.8$ s to $T_0 + 0.9$ s, the same procedure with the 30.5 GeV photon gives $\Gamma_{\rm min} \cong 1370$ or 1060 for $f_{-5} \approx 0.5$ or $f_{-5} \approx 0.1$ corresponding, respectively, to the combined Band plus power-law fit or the power-law component only.

The results of numerical integrations to determine $\Gamma_{\rm min}$ using the more detailed expressions in Abdo et al. (2009c) are shown in Table 2. As can be seen, the simple estimates given above are in good agreement with the detailed calculation. A number of issues arise in the use of Equation (6) or the numerical integrations that are important for assessing the value and uncertainty in $\Gamma_{\rm min}$. These include the error incurred by the uncertainties in source spectral fitting parameters, which properly involves a covariance matrix to correlate uncertainties for different parameters of the Band-function and power-law fit.

For $E_{\rm max}$, we take the highest energy photon associated with that pulse. Table 2 presents the values for t_v, $E_{\rm max}$, and $\Gamma_{\rm min}$ for time intervals $T_0 + 0.6$ s to $T_0 + 0.8$ s and $T_0 + 0.8$ s to $T_0 + 0.9$ s, which are the only two for which a distinct pulse width could be measured. In interval $T_0 + 0.6$ s to $T_0 + 0.8$ s, the Band + PL fit shown in Table 3 form the target photon spectrum, while in interval $T_0 + 0.8$ s to $T_0 + 0.9$ s, we present results for both the Band and Band + PL fits since each fits the data reasonably well. We also give values for $\Gamma_{\rm min}$ assuming that only the hard power-law component forms the target photon source. Here, we assume that t_v is the same as that measured from the BGO emission, which is primarily associated with photons in the Band portion of the spectrum. If the variability timescale of the power-law emission is different than assumed, which would be compatible with the two components originating from different locations, then the minimum Doppler factor limit would change as indicated by Equation (6). Furthermore, for calculations of $\Gamma_{\rm min}$ we use the spectrum derived on 0.2 s (time interval b) and 0.1 s (time interval c) timescales rather than on the shorter variability timescales during which the high-energy photons are measured. This is required for accurate spectral analysis, but could underestimate the flux (and therefore $\Gamma_{\rm min}$) during the bright narrow spikes, as can be seen from Figure 1.

The derivation of $\Gamma_{\rm min}$ crucially depends on the assumption that the high-energy radiation and target photons are made in the same emitting region. Correlated variability between different wavebands would support the cospatial assumption (see Figure 1), but no strong evidence for this behavior was found in the CCF analysis described in Section 3. A conservative assumption would be to suppose that the high-energy photon is part of the power-law component and that it can potentially interact only with target photons that are part of the same power-law emission component. Even in cases where the target MeV photons are made at smaller radii than the high-energy photons, or in different regions within the Doppler cone of the emitting surface, spacetime overlap will add to opacity, so this should represent the most conservative assumption. Further complicating the derivation of $\Gamma_{\rm min}$ is the assumed emitting geometry and the temporal evolution of the radiating plasma. For a blast-wave geometry, the precise value of $\Gamma_{\rm min}$ depends on whether high-energy photons are produced throughout the "shell" or from the inner edge of the "shell," and on the dynamical behavior of the target photons (Granot et al. 2008).

Finally, a significant uncertainty on $\Gamma_{\rm min}$ can arise if the photon with observed energy $E_{\rm max}$ is a random fluctuation of the underlying true spectrum that corresponds to $\Gamma \lesssim \Gamma_{\rm min}$ and $\tau_{\gamma\gamma}(E_{\rm max}) \gtrsim 1$. The confidence we have on the value of Γ depends on the radiative transport and escape of γ rays from the emitting region. For interval c from $T_0 + 0.8$ s to $T_0 + 0.9$ s, $\Gamma_{\rm min} = 1218 \pm 61$ for the Band plus power-law fit (Table 2). Assuming that the intrinsic spectrum extrapolates as a power law to high energies, a likelihood ratio test assuming an exponential escape probability gives $\Gamma/\Gamma_{\rm min} = 0.96$, 0.88, and 0.80 and

a spherical escape probability gives $\Gamma/\Gamma_{\rm min} = 0.89$, 0.69, and 0.49 at the 1σ, 2σ, and 3σ confidence levels, respectively. The presence of two photons with energies between 1 and 2 GeV in interval b and a 7 GeV photon in interval c reduces the likelihood that the highest energy photon is a fluctuation and can be used to independently estimate $\Gamma_{\rm min}$, giving a value $\Gamma_{\rm min} \gtrsim 1000$.

GRB 090510 is the second short GRB observed with LAT, after GRB 081024B (Abdo et al. 2010), but the first with a redshift, which is required to derive $\Gamma_{\rm min}$. The value of $\Gamma_{\rm min} \cong$ 1200–1300 for GRB 090510 is comparable to, and slightly larger than the values of $\Gamma_{\rm min} \cong 900$ and $\Gamma_{\rm min} \cong 1000$ derived for GRB 080916C (Abdo et al. 2009c) and GRB 090902B (Abdo et al. 2009b) using corresponding $\gamma\gamma$ opacity arguments. This has led to suggestions that the GRBs with the most luminous LAT emission are those with the largest bulk Lorentz factors (Kumar & Barniol Duran 2009b; Ghirlanda et al. 2010).

5.2. Models for the Prompt Radiation from GRB 090510

In addition to the requirement of bulk outflow Lorentz factors $\Gamma \gtrsim \Gamma_{\rm min}$, models for GRB 090510 should explain the $\approx$0.2 s delay of the onset of the $\gtrsim$100 MeV emission compared to the start of the main GBM emission at $T_0 + 0.5$ s, the appearance of a hard component, and the high-energy radiation extending to $\approx T_0 + 150$ s.

5.2.1. Synchrotron/SSC Model

A standard GRB model for the prompt phase assumes that the keV–MeV emission is nonthermal synchrotron radiation from shock-accelerated electrons (e.g., Tavani 1996). This emission is necessarily accompanied by SSC radiation.

The SSC component is stronger for a large ratio of nonthermal electron to magnetic field energy density, as expressed by the condition $\epsilon_e \gg \epsilon_B$ (Sari & Esin 2001; Zhang & Mészáros 2001), and also when the GRB has a lower bulk Lorentz factor for an external shock origin. Here, ϵ_e and ϵ_B are the fractions of shocked energy transferred to nonthermal lepton and magnetic field energy, respectively. Lower bulk Lorentz factors that give stronger SSC components result in greater attenuation of high-energy γ rays from $\gamma\gamma$ pair-production processes, as discussed in Section 5.1. For generic ($E_{\rm iso} \sim 10^{52}$ erg, $\Gamma_0 \sim 300$, $n \sim 1$ cm^{-3}) parameters expected in an external shock model, a hardening of the LAT spectrum due to the deceleration of the blast wave and the emergence of the SSC component in the LAT band was expected to take place in the afterglow phase, but not in the prompt phase (Dermer et al. 2000). With the larger initial Lorentz factors $\Gamma_0 \gtrsim 10^3$ implied by $\gamma\gamma$ arguments for LAT GRBs and the earlier emergence of an external shock component, an SSC component would persist after the decline of the synchrotron component due to less scattering taking place in the Klein–Nishina regime as the blast wave decelerates, and to the peak frequency of the SSC flux decreasing from the TeV to the GeV range. The detailed observations of GRB 090510 can help determine whether the hard power-law component appearing at $\approx T_0 + 0.7$ s can be explained by SSC emission in the LAT waveband during the prompt phase.

Figure 6 shows results for a numerical model where synchrotron peak energy, peak flux, and variability time are made to correspond to the observed values shown in Figure 5. This code employs a Compton kernel that accurately treats Compton-scattering of relativistic electrons throughout the Thomson and

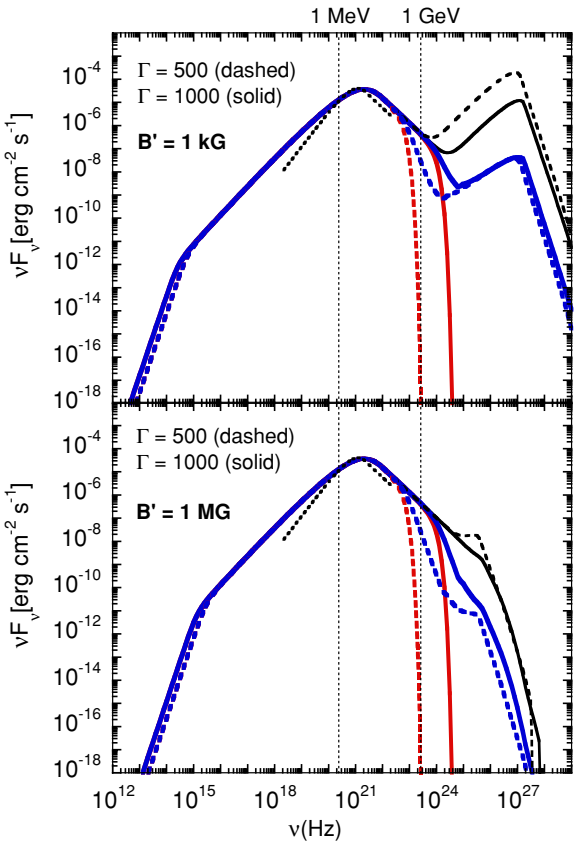

Figure 6. Synchrotron/SSC model for interval b ($T_0+0.6$ s to $T_0+0.8$ s) of GRB 090510. Dotted curves show the Band component during this time interval. The magnetic field in the top and bottom panels is 1 kG and 1 MG, respectively. The dashed and solid curves show results for $\Gamma = 500$ and $\Gamma = 1000$, respectively. The upper blue and lower red curves show received fluxes (without EBL corrections) assuming spherical and exponential γ-ray escape probabilities, respectively.

(A color version of this figure is available in the online journal.)

Klein–Nishina regimes, internal $\gamma\gamma$ opacity, synchrotron self-absorption, radiative escape for γ rays described by exponential and spherical escape probabilities, and second-order SSC. The code does not include reprocessing of internally absorbed radiation or effects of attenuation of γ-ray photons by the EBL (see Section 5.3). Parameters appropriate to the Band component in interval b (see Figures 1 and 5) are used, as shown by the dotted curves. The parameters are $t_v = 14$ ms, $E_{\rm peak} = 5.10$ MeV, $E_{\rm max} = 3.4$ GeV, $\alpha = -0.48$, $\beta = -3.09$, and peak synchrotron flux $\approx 4 \times 10^{-5}$ erg cm^{-2} s^{-1} (see Figure 5 and Tables 2 and 3). Figure 6 shows results for $\Gamma = 500$ (dashed curves) and $\Gamma = 1000$ (solid curves), and for magnetic fields $B' = 1$ kG and $B' = 1$ MG in the upper and lower panels, respectively. Note that subtraction of an underlying hard component will not change the peak νF_ν flux value by more than $\approx$5%.

The unattenuated power of the SSC component is comparable to the synchrotron power when $B' = 1$ kG, whereas the SSC component is much weaker in the strong-field case. The isotropic jet power for the $B' = 1$ kG model is $\cong 2.0 \times 10^{54}$ erg s^{-1} and $\cong 5.8 \times 10^{53}$ erg s^{-1} for $\Gamma = 500$ and $\Gamma = 1000$, respectively, and is dominated by the energy in the escaping radiation. When $B' = 1$ MG, the isotropic jet power is $\cong 1.1 \times 10^{55}$ erg s^{-1} and $\cong 7 \times 10^{56}$ erg s^{-1} for $\Gamma = 500$ and $\Gamma = 1000$, respectively, and is dominated by magnetic field energy. For $B' \ll 1$ kG, the SSC flux becomes much brighter than the synchrotron flux, and

the jet power becomes dominated by particles, even assuming that all particle energy is in the form of relativistic electrons.

Because the SSC component is strongly attenuated by $\gamma\gamma$ processes for the Γ factors considered, an electromagnetic cascade will be formed with γ rays emerging at lower energies where the system becomes optically thin. The timescale for the electromagnetic radiation to cascade to energy E_γ is shorter than the synchrotron time, given by $t_{\rm syn} \approx 0.006(\Gamma/1000)^{1/2}/((B'/{\rm kG})^{3/2}\sqrt{E_\gamma/100\ {\rm MeV}})$ s. Unless $B' \ll 1$ kG, in which case much more power is found in the cascading SSC emission than in the synchrotron emission, the cascading timescale is too short to explain the $\approx$0.2 s delay between the GBM and LAT emission. This model also faces the well-known line-of-death problem (Preece et al. 1998) that the standard synchrotron mechanism makes a spectrum softer than $\alpha = -2/3$, whereas $\alpha = -0.48 \pm 0.07$ in interval b, representing a nearly 3σ discrepancy from the hardest expected synchrotron emissivity. For the strong-field case where the SSC component is weak, the separate hard component in GRB 090510 would then have to originate from a different mechanism.

5.2.2. Afterglow Synchrotron Model

Kumar & Barniol Duran (2009a, 2009b) and Ghirlanda et al. (2010); Ghisellini et al. (2010) have proposed forward shock emission from the early afterglow as the origin of the delayed onset and the hard component extending into the LAT energy band. This possibility is also considered by De Pasquale et al. (2010), Corsi et al. (2009), and Gao et al. (2009). In particular, Ghirlanda et al. (2010) calculate the coasting bulk Lorentz factor of the GRB jet by identifying the time of the peak LAT emission occurring at $\approx T_0 + 0.7$ s with the deceleration time of a relativistic blast wave. If η is the efficiency to convert bulk kinetic energy to γ-ray energy, $\Gamma_0 \approx 2000 n^{-1/8}(t_{\rm peak}/0.2\ {\rm s})^{-3/8}(\eta/0.2)^{-1/8}(E_{\gamma,{\rm iso}}/3.5\times10^{52}\ {\rm erg})^{1/8}$, where n (cm^{-3}) is the density of the surrounding medium. This expression uses an apparent isotropic γ-ray energy release that excludes the LAT emission, which if due to synchrotron radiation from relativistic electrons, would require a radiative efficiency approaching unity.

Depending on circumburst density, the implied Lorentz factor is about 2–4 times the value of $\Gamma_{\rm min}$ calculated in the previous section. For this model, the emission radius corresponding to the time of the peak LAT flux is $R \approx 2.4 \times 10^{16} n^{-1/4}$ cm. At $t \approx t_{\rm peak}$, the minimum energy electrons in the forward shock radiate synchrotron photons at energies $h\nu_m \approx 3.6(\epsilon_e/0.1)^2\xi_e^{-2}(\epsilon_B/0.01)^{1/2}E_{53}^{1/2}(t/0.2\,{\rm s})^{-3/2}$ MeV assuming an electron injection index of $p \approx 2.4$, where ξ_e is the fraction of the electrons that take part in the non-thermal power-law component responsible for the observed emission.

Recent particle in cell simulations of relativistic collisionless shocks (Spitkovsky 2008a, 2008b; Martins et al. 2009) suggest that ξ_e is fairly small (of the order of a few percent), which may in our case allow $h\nu_m$ of several MeV even for low values of ϵ_B. For $\epsilon_e = 0.1$, $\epsilon_B = 0.01$, and an isotropic equivalent kinetic energy of $E_{k,{\rm iso}} = 10^{53}$ erg (similar to $E_{\gamma,{\rm iso}}$), the cooling break frequency is given by (Granot & Sari 2002), $h\nu_c \approx 0.4 n^{-1}(\epsilon_e/0.1)^{-1}(\epsilon_B/0.01)^{-1/2}E_{53}^{-1/2}(t/0.2\ {\rm s})^{-1/2}$ keV. This expression holds when $\epsilon_B \ll \epsilon_e$ and Klein–Nishina effects are unimportant, so that $Y = ((1+4\epsilon_e/\epsilon_B)^{1/2} - 1)/2 \approx \sqrt{\epsilon_e/\epsilon_B} > 1$. This would imply fast cooling $\nu_c \ll \nu_m$ for $n \sim 1$, which could result in a highly radiative shock for $\epsilon_e \sim 1$. However, the late time broadband spectrum at $t \sim 100$ s from optical–UV through X-ray and up to the LAT γ-ray energies (De Pasquale et al. 2010) suggests $h\nu_c(100\,{\rm s}) \sim 300$ MeV, which, even if with a large uncertainty, together with the overall afterglow modeling suggests a much lower external density of $n \sim 10^{-5}$. Such a low density would imply $h\nu_c \approx 0.3(n/10^{-5})^{-1}(\epsilon_B/0.01)^{-3/2}E_{53}^{-1/2}(t/0.5\ {\rm s})^{-1/2}$ GeV (where the Klein–Nishina effect suppresses SSC cooling), so that ν_c passes through the (low part of the) LAT energy range around $\sim$0.5 s from the onset of the main emission episode, or at $\sim T_0 + 1$ s, when there is a softening in the LAT photon index, near the end of the prompt emission. Thus, after the prompt emission, the LAT energy range would be above both ν_m and ν_c, accounting for the observed photon index. This would imply $h\nu_c \approx 18(n/10^{-5})^{-1}(\epsilon_B/0.01)^{-3/2}E_{53}^{-1/2}(t/100\ {\rm s})^{-1/2}$ MeV which is consistent with the broadband spectrum at that time, especially since the spectral break around ν_c is very smooth and gradual (Granot & Sari 2002). Interestingly, the inferred value of $h\nu_m(100\,{\rm s}) \approx 0.43$ keV and the $\nu_m \propto t^{-3/2}$ scaling gives $h\nu_m(t_{\rm peak} \approx 0.2\,{\rm s}) \approx 4.8$ MeV, which is very close to the measured value of $E_{\rm peak}$ near $t_{\rm peak}$. This model would not produce a spectrum softer than $\nu F_\nu \propto \nu^{4/3}$, so would have difficulty accounting for the emission near 10 keV in interval b, which appears to be a continuation of the hard spectral component.

For an adiabatic blast wave and an electron injection index p, the synchrotron flux scales as $\nu F_\nu \propto t^{(2-3p)/4}\nu^{(2-p)/2}$ at frequencies $\nu > \nu_m, \nu_c$. The measured late time LAT flux decay rate of $\nu F_\nu \propto t^{-1.38\pm0.07}\nu^{-0.1\pm0.1}$ would in this case require $p = 2.5 \pm 0.1$, while the spectral slope requires $p = 2.2 \pm 0.2$. Both are consistent with $p = 2.4$ at the 1σ level. This value is also consistent with the late time afterglow of GRB 090510 (De Pasquale et al. 2010). A radiative blast wave at early times is not required in order to account for the observed early LAT flux decay rate.

5.2.3. Hadronic Models

In hadronic models, photohadronic and proton/ion synchrotron processes induce electromagnetic cascades, which lead to synchrotron and Compton emissions from secondary electron–positron pairs (e.g., Dermer & Atoyan 2006; Gupta & Zhang 2007; Asano & Inoue 2007). For a target photon energy distribution $n(\epsilon) \propto \epsilon^x$, the efficiency for photopion processes is $\propto R^{-1}\Gamma^{-2}E_{\rm p}^{-1-x} \propto \Gamma^{-4}t_{\rm v}^{-1}E_{\rm p}^{-1-x}$, where $R \propto c\Gamma^2 t_{\rm v}$ is the shock radius. In this expression, protons with energy $E_{\rm p}$ preferentially interact with photons with energies $\propto \Gamma^2/E_{\rm p}$ (Waxman 1995; Murase 2009). The large deduced values for Γ in GRB 090510 make the photopion efficiency low, so that a very large energy release is required if the LAT radiation from GRB 090510 is assumed to be from a photomeson-induced cascade.

A stronger magnetic field shortens the acceleration timescale, leading to a larger maximum particle energy $E_{\rm max}$, thus enhancing the photopion production efficiency. In such a strong magnetic field, however, the effective injection index of secondary pairs tends to be about -2 (Coppi 1992), which yields a flat spectrum in a νF_ν plot, while the power-law index of the extra component in GRB 090510 is ~ -1.6. In a weaker magnetic field, the Compton component from secondary pairs can harden the spectrum, though with reduced photopion production efficiency due to the smaller value of $E_{\rm max}$. The slower cooling time of protons than electrons would produce an extended proton-induced emission feature (Böttcher & Dermer 1998), though the SSC component would decay even more slowly (Zhang

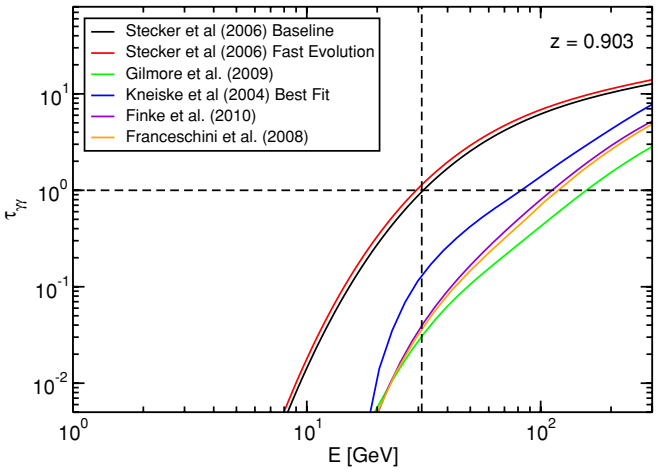

Figure 7. Model predictions of EBL absorption optical depth vs. photon energy for GRB 090510. The dashed horizontal line indicates an optical depth of unity, and the dashed vertical line shows the energy of the highest energy photon.
(A color version of this figure is available in the online journal.)

& Mészáros 2001). A recent numerical calculation by Asano et al. (2009) for GRB 090510 demonstrates that the proton injection isotropic-equivalent power is required to be larger than 10^{55} erg s^{-1} to explain the hard spectra of the extra component in GRB 090510, which is ≈2 orders of magnitude greater than the measured apparent isotropic γ-ray luminosity.

An alternative hadronic scenario is a proton synchrotron model with a very strong magnetic field (Razzaque et al. 2009). This model explains the delayed onset by proton synchrotron radiation in the prompt phase due to the time required to accelerate, accumulate, and cool the ultrarelativistic protons. For an onset time $t_{\rm onset} \approx 0.2$ s after the start of the GBM main emission at $T_0 + 0.5$ s, the required magnetic field is $B' \approx 7.4 \times 10^5 (\Gamma/1000)^{-1/3} (t_{\rm onset}/0.1\ {\rm s})^{-2/3} ({\rm E}_\gamma/100\,{\rm MeV})^{-1/3}$ G in the shocked fluid frame. The corresponding total energy release, for a two-sided jet beaming factor $f_b \approx 1.5 \times 10^{-4} (\theta_j/1\,{\rm deg})^2$, is $\mathcal{E} \approx 1.3 \times 10^{54} (\Gamma/1000)^{16/3} (t_{\rm onset}/0.1\ {\rm s})^{5/3} (E_\gamma/100\ {\rm MeV})^{-2/3} (\theta_{\rm j}/1\ {\rm deg})^2$ erg (see Wang et al. 2009, for GRB 080916C). Thus values of $\Gamma \lesssim 1000$ and narrow jet angles ≈1° are required for a proton synchrotron scenario, and such strong beaming is not clearly found in the short–hard class of GRBs (Nakar 2007). Proton-dominated GRB models for ultra-high energy cosmic rays therefore are plausible only with low values of Γ and narrow jet collimation to reduce the total energy.

5.3. Implications for the Extragalactic Background Light

The EBL is dominated by direct starlight in the optical/ultraviolet and by stellar radiation that is reprocessed by dust in the infrared. The EBL is difficult to measure directly due to contamination by zodiacal and Galactic foreground light (Hauser & Dwek 2001). For sources at sufficiently high redshifts, $\gamma\gamma$ absorption of high-energy γ rays by EBL photons can provide a means of constraining models of the EBL. Figure 7 shows the absorption optical depth, $\tau_{\gamma\gamma}$, for various models of the EBL as a function of γ-ray energy at the redshift $z = 0.903$ of GRB 090510.

We have included curves for the two models of Stecker et al. (2006) as well as the fiducial model of Gilmore et al. (2009), the best-fit model of Kneiske et al. (2004), the model by Franceschini et al. (2008), and "Model C" of Finke et al. (2010). The models of Stecker et al. (2006) border on optically thick at 30.5 GeV; all other models considered here give a transmission probability of $e^{-\tau_{\gamma\gamma}} \gtrsim 0.85$. The baseline and fast evolution models of Stecker et al. (2006) give transmission probabilities of 0.37 and 0.30, respectively. Although a higher energy (≈30.5 GeV) photon was found from this burst than for GRB 080916C (13 GeV; Abdo et al. (2009c)), that burst was more constraining for EBL models due to its higher redshift, $z = 4.35 \pm 0.15$ (Greiner et al. 2009). However, the EBL does evolve with redshift, and this GRB provides an independent constraint from a later time and at a closer distance than GRB 080916C. The low optical depth for the highest energy photons in GRB 090510 justify neglecting EBL effects in Figure 6.

6. SUMMARY

We have presented *Fermi* observations of the short–hard GRB 090510 during the prompt emission phase extending to 3 s after the GRB trigger (*Fermi* and *Swift* observations at later times are presented in De Pasquale et al. 2010). The apparent isotropic energy measured by the *Fermi* GBM and LAT from GRB 090510 is $(1.08 \pm 0.06) \times 10^{53}$ erg in the energy range from 10 keV to 30 GeV, where the upper limit is defined by the highest energy photon. When corrected for corresponding energy ranges, this is at least an order of magnitude greater than the isotropic energy releases measured from *Swift* GRBs with known redshift (Nakar 2007), indicating that GRB 090510 is unusually energetic. A faint precursor and one LAT photon with energy >100 MeV are observed ≈0.5 s before the main pulse, and two other LAT photons are detected before the start of the bright GBM emission. Large numbers of >100 MeV LAT photons are detected beginning at $\approx T_0 + 0.7$ s.

Spectral analysis shows that the time-integrated flux cannot be fit with a single Band spectrum, but is well fit with a power-law emission component in addition to the Band component. In the time interval $T_0 + 0.6$ s to $T_0 + 0.8$ s, the GRB emission can be resolved into a Band function with $\alpha = -0.48 \pm 0.07$ and a hard spectral power law with number index $= -1.66$. The GBM emission is observed to vary on a timescale of 14 ± 2 ms in this interval, and on a timescale of 12 ± 2 ms in the time interval c, from $T_0 + 0.8$ s to $T_0 + 0.9$ s. Our results are summarized in Table 2. In time interval c, where the highest energy (≈30.5 GeV) photon is detected, our most conservative assumptions give $\Gamma \gtrsim 1000$.

We considered models for the delayed onset of the high-energy LAT radiation and the appearance of the distinct hard spectral component. In particular, we considered whether the emission spectrum can be explained by a synchrotron model for the Band function and SSC emission for the hard power-law component in the GeV range. Cascading of SSC emission into the LAT range from higher energies could explain the hard component, but the delayed onset is found to be too long compared to the time for development of the cascade. Moreover, the hard GBM spectrum presents a challenge for synchrotron models that could instead be explained by a photospheric emission component. Other models, including external-shock synchrotron and hadronic models, are also considered to explain the *Fermi* observations of GRB 090510. Future *Fermi* observations of short GRBs will help to discriminate between models and improve our understanding of relativistic outflows in GRBs.

We thank the anonymous referee for a careful reading of the manuscript and for many helpful suggestions that have improved the paper.

The *Fermi* LAT Collaboration acknowledges generous ongoing support from a number of agencies and institutes that have supported both the development and the operation of the LAT as well as scientific data analysis. These include the National Aeronautics and Space Administration and the Department of Energy in the United States, the Commissariat à l'Energie Atomique and the Centre National de la Recherche Scientifique/Institut National de Physique Nucléaire et de Physique des Particules in France, the Agenzia Spaziale Italiana and the Istituto Nazionale di Fisica Nucleare in Italy, the Ministry of Education, Culture, Sports, Science and Technology (MEXT), High Energy Accelerator Research Organization (KEK) and Japan Aerospace Exploration Agency (JAXA) in Japan, and the K. A. Wallenberg Foundation, the Swedish Research Council and the Swedish National Space Board in Sweden.

Additional support for science analysis during the operations phase is gratefully acknowledged from the Istituto Nazionale di Astrofisica in Italy and the Centre National d'Études Spatiales in France.

The *Fermi* GBM Collaboration acknowledges support for GBM development, operations, and data analysis from NASA in the US and BMWi/DLR in Germany.

REFERENCES

Abdo, A. A., et al. 2009a, Nature, 462, 331
Abdo, A. A., et al. 2009b, ApJ, 706, L138
Abdo, A. A., et al. 2009c, Science, 323, 1688
Abdo, A. A., et al. 2010, ApJ, 712, 558
Asano, K., Guiriec, S., & Mészáros, P. 2009, ApJ, 705, L191
Asano, K., & Inoue, S. 2007, ApJ, 671, 645
Atwood, W. B., et al. 2009, ApJ, 697, 1071
Band, D., et al. 1993, ApJ, 413, 281
Baring, M. G., & Harding, A. K. 1997, ApJ, 491, 663
Berger, E. 2009, ApJ, 690, 231
Böttcher, M., & Dermer, C. D. 1998, ApJ, 499, L131
Coppi, P. S. 1992, MNRAS, 258, 657
Corsi, A., Guetta, D., & Piro, L. 2009, arXiv:0911.4453
De Pasquale, M., et al. 2010, ApJ, 709, L146
Dermer, C. D., & Atoyan, A. 2006, New J. Phys., 8, 122
Dermer, C. D., Chiang, J., & Mitman, K. E. 2000, ApJ, 537, 785
Dondi, L., & Ghisellini, G. 1995, MNRAS, 273, 583
Finke, J. D., Razzaque, S., & Dermer, C. D. 2010, ApJ, 712, 238
Frail, D. A., & Chandra, P. 2009, GRB Coordinates Network, 9354, 1
Franceschini, A., Rodighiero, G., & Vaccari, M. 2008, A&A, 487, 837
Gao, W., Mao, J., Xu, D., & Fan, Y. 2009, ApJ, 706, L33
Ghirlanda, G., Ghisellini, G., & Nava, L. 2010, A&A, 510, L7
Ghisellini, G., Ghirlanda, G., Nava, L., & Celotti, A. 2010, MNRAS, 403, 926
Gilmore, R. C., Madau, P., Primack, J. R., Somerville, R. S., & Haardt, F. 2009, MNRAS, 399, 1694
Golenetskii, S., et al. 2009, GRB Coordinates Network, 9344, 1
González, M. M., Dingus, B. L., Kaneko, Y., Preece, R. D., Dermer, C. D., & Briggs, M. S. 2003, Nature, 424, 749
Granot, J., Cohen-Tanugi, J., & do Couto e Silva, E. 2008, ApJ, 677, 92
Granot, J., & Sari, R. 2002, ApJ, 568, 820
Greiner, J., et al. 2009, A&A, 498, 89
Gupta, N., & Zhang, B. 2007, MNRAS, 380, 78
Hauser, M. G., & Dwek, E. 2001, ARA&A, 39, 249
Hoversten, E. A., et al. 2009, GRB Coordinates Network, 9331, 1
Hurley, K., et al. 1994, Nature, 372, 652
Kneiske, T. M., Bretz, T., Mannheim, K., & Hartmann, D. H. 2004, A&A, 413, 807
Kocevski, D., West, A. A., & Modjaz, M. 2009, ApJ, 702, 377
Koshut, T. M., Paciesas, W. S., Kouveliotou, C., van Paradijs, J., Pendleton, G. N., Fishman, G. J., & Meegan, C. A. 1996, ApJ, 463, 570
Kouveliotou, C., Meegan, C. A., Fishman, G. J., Bhat, N. P., Briggs, M. S., Koshut, T. M., Paciesas, W. S., & Pendleton, G. N. 1993, ApJ, 413, L101
Kuin, N. P. M., & Hoversten, E. A. 2009, GRB Coordinates Network, 9342, 1
Kumar, P., & Barniol Duran, R. 2009a, arXiv:0910.5726
Kumar, P., & Barniol Duran, R. 2009b, MNRAS, 400, L75
Lee, W. H., & Ramirez-Ruiz, E. 2007, New J. Phys., 9, 17
Lithwick, Y., & Sari, R. 2001, ApJ, 555, 540
Longo, F., et al. 2009, GRB Coordinates Network, 9343, 1
Lyutikov, M., & Blandford, R. 2003, arXiv:astro-ph/0312347
Martins, S. F., Fonseca, R. A., Silva, L. O., & Mori, W. B. 2009, ApJ, 695, L189
McBreen, S., et al. 2010, A&A, in press (arXiv:1003.3885)
Mészáros, P., Ramirez-Ruiz, E., Rees, M. J., & Zhang, B. 2002, ApJ, 578, 812
Murase, K. 2009, Phys. Rev. Lett., 103, 081102
Nakar, E. 2007, Phys. Rep., 442, 166
Norris, J. P., & Bonnell, J. T. 2006, ApJ, 643, 266
Norris, J. P., Marani, G. F., & Bonnell, J. T. 2000, ApJ, 534, 248
Ohmori, N., et al. 2009, GRB Coordinates Network, 9355, 1
Olivares, F., Klose, S., Kruehler, T., & Greiner, J. 2009, GRB Coordinates Network, 9352, 1
Olofsson, G., Ergon, M., Malesani, D., Fynbo, J. P. U., Jakobsson, P., Tanvir, N. R., Wiersema, K., & Levan, A. J. 2009, GRB Coordinates Network, 9338, 1
Pe'er, A., Ryde, F., Wijers, R. A. M. J., Mészáros, P., & Rees, M. J. 2007, ApJ, 664, L1
Preece, R. D., Briggs, M. S., Mallozzi, R. S., Pendleton, G. N., Paciesas, W. S., & Band, D. L. 1998, ApJ, 506, L23
Rau, A., McBreen, S., & Kruehler, T. 2009, GRB Coordinates Network, 9353, 1
Razzaque, S., Dermer, C. D., & Finke, J. D. 2009, arXiv:0908.0513
Razzaque, S., Mészáros, P., & Zhang, B. 2004, ApJ, 613, 1072
Sari, R., & Esin, A. A. 2001, ApJ, 548, 787
Sari, R., Piran, T., & Narayan, R. 1998, ApJ, 497, L17
Spitkovsky, A. 2008a, ApJ, 673, L39
Spitkovsky, A. 2008b, ApJ, 682, L5
Stecker, F. W., Malkan, M. A., & Scully, S. T. 2006, ApJ, 648, 774
Tavani, M. 1996, Phys. Rev. Lett., 76, 3478
Toma, K., Wu, X., & Meszaros, P. 2010, arXiv:1002.2634
Wang, X., Li, Z., Dai, Z., & Mészáros, P. 2009, ApJ, 698, L98
Waxman, E. 1995, Phys. Rev. Lett., 75, 386
Woosley, S. E., & Bloom, J. S. 2006, ARA&A, 44, 507
Zhang, B., & Mészáros, P. 2001, ApJ, 559, 110